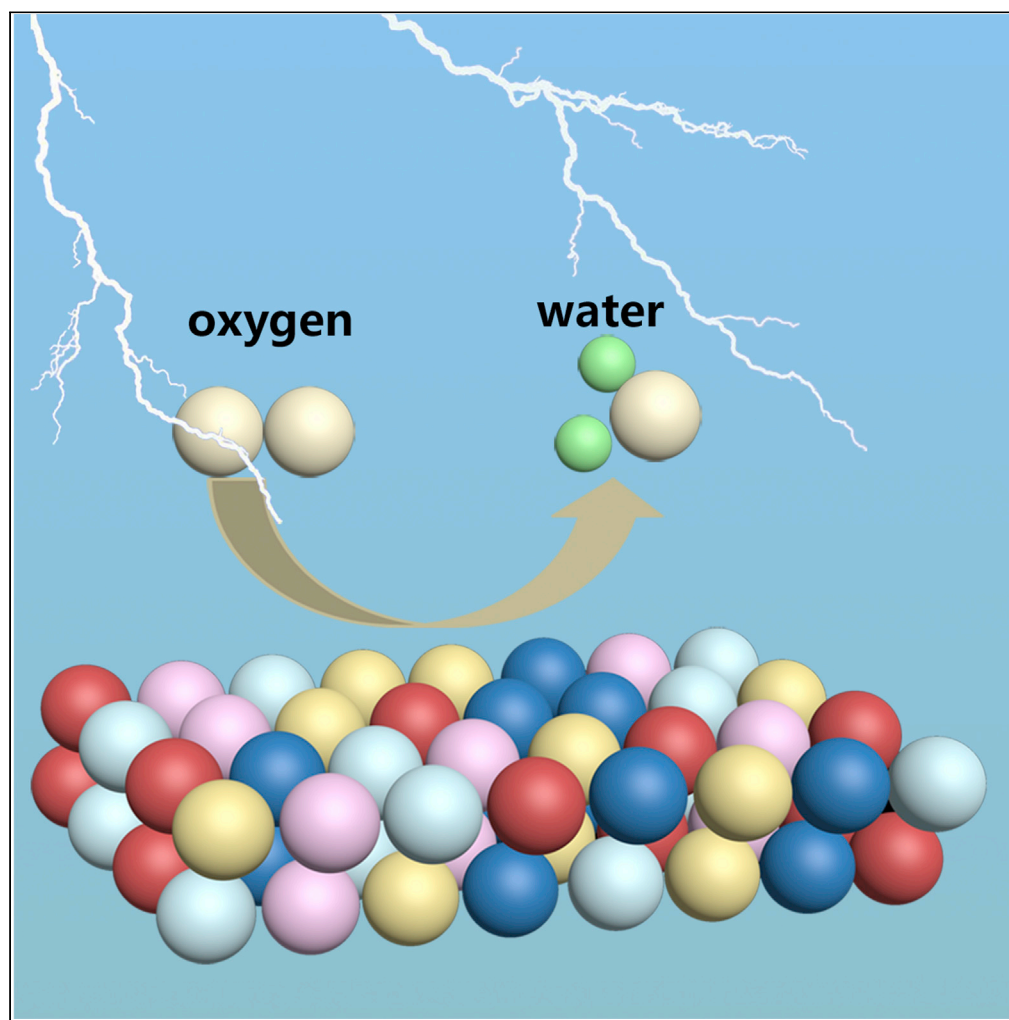**Article**

PtFeCoNiCu high-entropy solid solution alloy as highly efficient electrocatalyst for the oxygen reduction reaction

Tao Chen,
Fanghua Ning,
Jizhen Qi, ..., Xi
Liu, Liwei Chen,
Dingguo Xia

lwchen2018@sjtu.edu.cn (L.C.)
dgxia@pku.edu.cn (D.X.)

Highlights

It promotes the formation of multiple ORR active sites to speed up the reaction rate

Multi-element alloying decreases the activation barriers for the O-O bond scission

It exhibits outstanding ORR activity and stability

It delivers the power density of up to 1.380 W cm^{-2} in fuel cell

Article

PtFeCoNiCu high-entropy solid solution alloy as highly efficient electrocatalyst for the oxygen reduction reaction

Tao Chen,[1,5] Fanghua Ning,[1,5] Jizhen Qi,[3,5] Guang Feng,[1] Yucheng Wang,[4] Jin Song,[1] Tonghuan Yang,[1] Xi Liu,[2] Liwei Chen,[2,*] and Dingguo Xia[1,6,*]

SUMMARY

Searching for an efficient, durable, and low cost catalyst toward oxygen reduction reaction (ORR) is of paramount importance for the application of fuel cell technology. Herein, PtFeCoNiCu high-entropy alloy nanoparticles (PFCNC-HEA) is reported as electrocatalyst toward ORR. It shows remarkable ORR catalytic mass activity of 1.738 A mg^{-1}_{Pt} at 0.90 V, which is 15.8 times higher than that of the state-of-art commercial Pt/C catalyst. It also exhibits outstanding stability with negligible voltage decay (3 mV) after 10k cycles accelerated durability test. High ORR activity is ascribed to the ligand effect caused by polymetallic elements, the optimization of the surface electronic structure, and the formation of multiple active sites on the surface. In the proton exchange membrane fuel cell setup, this cell delivers a power density of up to 1.380 W cm^{-2} with a cathodic Pt loading of 0.03 $mg_{Pt}\ cm^{-2}$, demonstrating a promising catalyst design direction for highly efficient ORR.

INTRODUCTION

Proton exchange membrane fuel cells (PEMFCs) convert chemical energy to electricity, which is considered to be a promising sustainable energy system owing to its sufficient energy conversion efficiency and environmentally friendly features.[1–4] Nevertheless, the sluggish kinetics of the oxygen reduction reaction (ORR) at the cathode hinder the application of PEMFCs.[5–9] Currently, Pt is still the most practical catalyst for the ORR, demonstrating promising activity.[10,11] Considering the scarcity of natural reserves, high cost, and poor electrochemical durability of Pt, the promotion of fuel cells remains challenging.[6,12,13] To reduce the use of Pt, considerable efforts have been contributed to enhancing the mass activity of Pt for the ORR. Alloying Pt with other non-noble metals is one of the most promising approaches for adjusting the d-band center of Pt to key intermediates to significantly promote the electrocatalytic performance of Pt-based electrocatalysts.[14,15] Although alloying technology has led to the design of ORR catalysts, the catalytic performance, and stability of these alloys have been considerably degraded owing to the continuous dissolution of the alloys during voltage cycling in acid.[12,16,17]

Recently, high-entropy alloys (HEAs) have emerged as promising multifunctional catalysts owing to the multiple active sites caused by multiple components.[18–22] By reasonably adjusting the composition and geometry of HEAs, it can not only optimize the electronic structure to a great extent but also construct catalysts with unexpected performance.[23,24] The "high entropy effect" resulting from the enhanced mixed configuration entropy of HEAs could improve the thermodynamic stability and corrosion properties of the catalyst.[25–30] Although HEA catalysts are promising, the exploration of HEA catalysts is still in its infancy, especially as an ORR catalyst in acidic electrolytes. At present, HEAs are mainly prepared by some complex, energy consuming, and time-consuming methods (such as carbon thermal shock method, extended mechanical ball milling, liquid metal dealloying, pulsed laser ablation, rapid moving bed paralysis, and so forth), which makes it urgent to develop simple and feasible preparation methods.[31] Furthermore, the complex catalytic mechanism of HEAs has not been deeply studied. Therefore, it is urgent to design more reasonable HEAs as a sufficiently advanced oxygen reduction catalyst, so as to accelerate the research of HEA catalysts in the field of acid electrocatalysis.

[1]Beijing Key Laboratory of Theory and Technology for Advanced Batteries Materials, School of Materials Science and Engineering, Peking University, Beijing 100871, PR China

[2]In-situ Center for Physical Sciences, School of Chemistry and Chemical Engineering, Shanghai Jiaotong University, Shanghai 200240, PR China

[3]I-Lab, CAS Center for Excellence in Nanoscience, Suzhou Institute of Nano-Tech and Nano Bionics, Chinese Academy of Sciences, Suzhou 215123, PR China

[4]State Key Laboratory of Physical Chemistry of Solid Surfaces, Collaborative Innovation Center of Chemistry for Energy Materials, College of Chemistry and Chemical Engineering, Xiamen University, Xiamen 361005, China

[5]These authors contributed equally

[6]Lead contact

*Correspondence:
lwchen2018@sjtu.edu.cn
(L.C.),
dgxia@pku.edu.cn (D.X.)
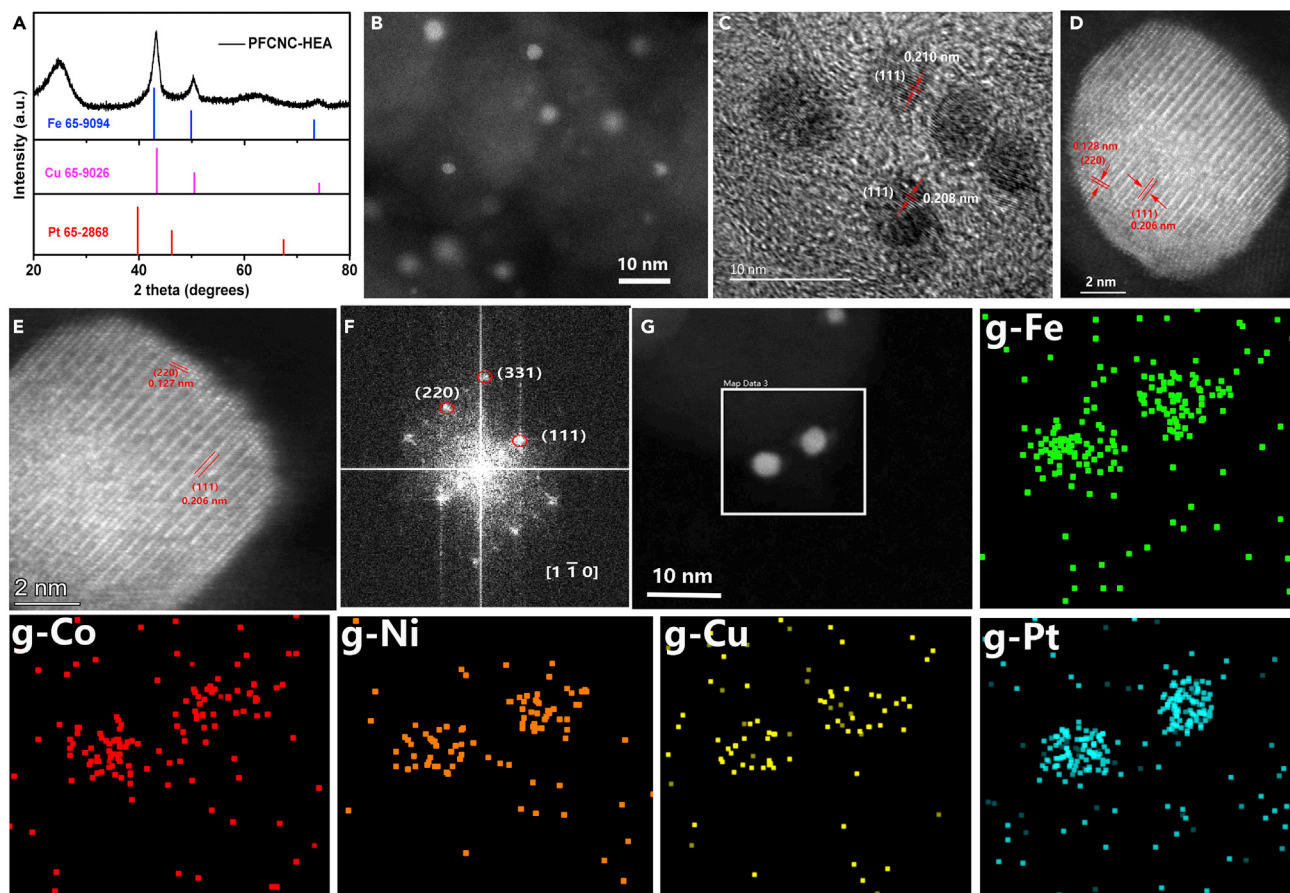https://doi.org/10.1016/j.isci.2022.105890

Figure 1. Morphology, structure, and composition characterization

(A) XRD pattern of PFCNC-HEAs.

(B) TEM image and (C) HR-TEM images of PFCNC-HEA nanoparticles.

(D and E) HAADF-STEM images of an individual PFCNC-HEA nanoparticle (F) Corresponding FFT pattern of (E).

(G) The corresponding elemental mapping of PFCNC-HEA nanoparticles.

Here, we report a PtFeCoNiCu high-entropy alloy (denoted as PFCNC-HEA) used as an ORR catalyst via an impregnation reduction method. The as-prepared PFCNC-HEA shows uniform dispersion and small particle size. It demonstrates outstanding ORR performance with mass activities of 1.738 A mg$^{-1}_{Pt}$ at 0.90 V vs. reversible hydrogen electrode (RHE), which is 15.8 times higher than that of the commercial Pt/C catalyst. It also exhibits superior cycling stability with negligible voltage decay (3 mV) after 10k cycles accelerated durability test and up to 90.23% maintaining of the initial current, far surpassing 55.34% of commercial Pt/C, after 40000s chronoamperometric measurements. Furthermore, the full cell, using the PFCNC-HEA as a cathode ORR catalyst, delivers a maximum power density of 1.38 W cm^{-2} with a cathodic Pt loading of 0.03 mg$_{Pt}$ cm^{-2} in PEMFCs. The results of DFT demonstrate that multi-element alloying decreases the activation barriers for the O-O bond scission and changes the binding energy of the *OOH intermediates to improve the reaction rate by combining metals with different affinities toward oxygen. In addition, multi-element alloying also promotes the formation of multiple ORR active sites to speed up the reaction rate. Thus, such a high-entropy solid solution alloy approach could be a promising method for ORR catalyst design.

RESULTS AND DISCUSSION

The ratio of Pt/Cu/Ni/Co/Fe atoms was determined to be 1.0:2.4:1.9:1.8:2.0 with a loading of 2 wt % Pt in PFCNC-HEA obtained by inductively coupled plasma-atomic emission spectroscopy (ICP-AES). The mixed configuration entropy of PFCNC-HEA is calculated to be 1.576R by Equation 1, which refers to a HEA. Such non-noble composition selection is based on the consideration of atomic radius, formation heat, and reported oxygen reduction activity of each component, in order to obtain high entropy solid solution alloy with high activity.[32–35] Figure 1A shows the powder X-ray diffraction (PXRD) pattern of the PFCNC-HEA,
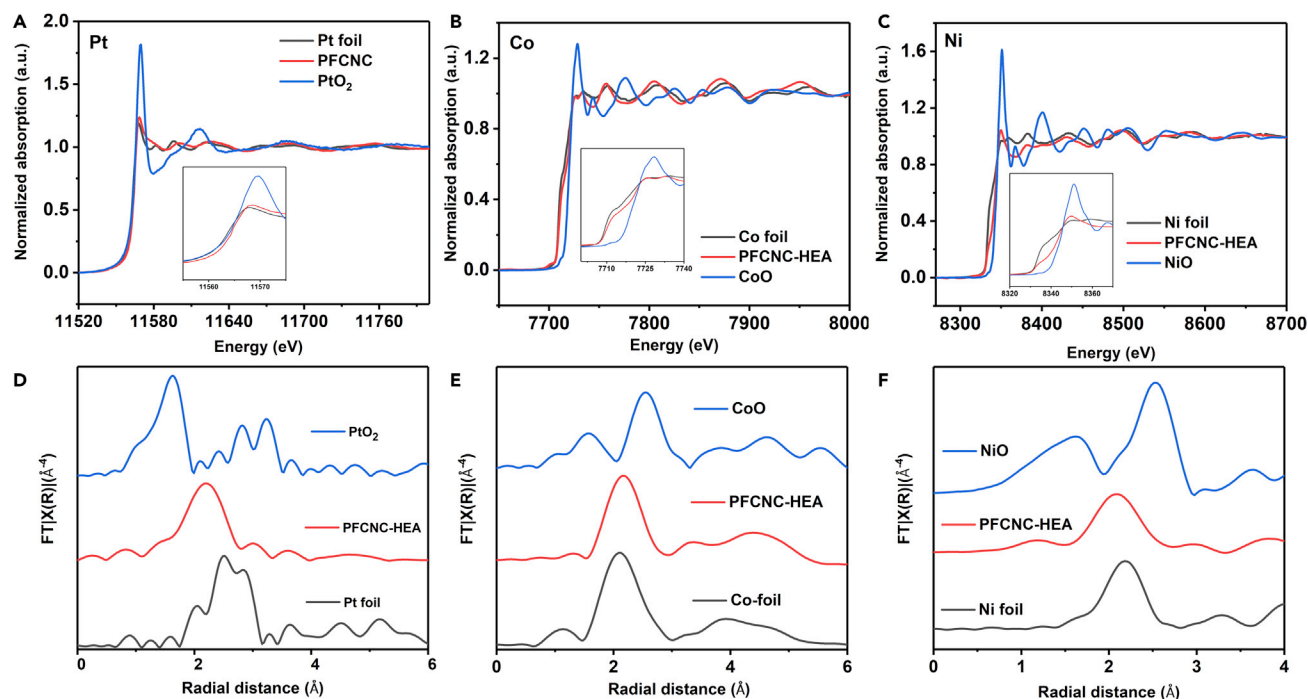
Figure 2. Characterization of electronic structure and coordination structure

L_3-edge XANES spectra of (A) Pt, and K-edge XANES spectra of (B) Co and (C) Ni elements in PFCNC-HEA nanoparticles. FT-EXAFS spectra of (D) Pt, (E) Co, and (F) Ni elements.

which can be indexed to face-centered cubic (fcc) structure with space group Fm $\overline{3}$ m (No. 225). The diffraction peaks shift to a high angle compared with that of pure Pt, Cu, and Fe, which is caused by multi-element alloying.[36] The typical transmission electron microscopy (TEM) image (Figure 1B) of PFCNC-HEA reveals highly dispersed nanoparticles of less than 5 nm in size. High-resolution transmission electron microscopy (HRTEM) images (Figure 1C) show a single-crystal structure with obvious lattice fringes. The lattice spacing is measured as about 0.208 nm that corresponds to the (111) plane of the face-centered cubic (fcc) structure. Figure 1G-Fe, Co, Ni, Cu, Pt show the elemental maps of PFCNC-HEA. It can be found that the five elements are evenly distributed in the nanoparticles of PFCNC-HEA, and no obvious segregation or phase separation is observed. In addition, the TEM-EDS measurement results (Figure S1) show that the content of each component is consistent with the range required by HEA. (that is, S $\geq$ 1.5R, where S represents the mixed configuration entropy and R is the molar gas constant).[37]

To further study the crystal structure of PFCNC-HEA, the high-angle annular dark-field scanning transmission electron microscopy (HAADF-STEM) images of individual nanoparticles are displayed in Figures 1D, 1E, and S2. The bright spots represent the atomic columns of the transition metal. Crystal layers with surface spacings of 0.127 nm and 0.206 nm are clearly observed, corresponding to the (220) and (111) of fcc structure, respectively. In addition, the same crystal plane can be observed in the corresponding fast Fourier transform FFT diagram in Figure 1F, which shows the atomic arrangement view along the [1 $\overline{1}$ 0] direction. The HAADF-STEM elemental maps of individual PFCNC-HEA nanoparticles (Figure S3) further confirm the successful high-entropy alloying of PFCNC-HEA at the particle level (Figure S4). The EDX line-scan profile of the PFCNC-HEA nanoparticle shows that each element uniformly distributes from the inside to the outside without delamination or segregation (Figure S5).

Figures 2A–2C, S6A, and S6B show the normalized Pt L3-edge, Co, Ni, Cu, Fe K-edge X-ray absorption near edge structure (XANES) spectra in PFCNC-HEA and relevant control samples. The "white line" (WL) intensity of XANES arises from the different electron occupancies of the d orbitals of the metal corresponding to the 2p → nd electronic transition. It can be found that the WL intensity of the absorption edge of Pt, Co, Ni, Fe, and Cu spectra in PFCNC-HEA are remarkably lower than that of PtO_2, CoO, NiO, FeO, and CuO, respectively, while the Pt, Co, Ni, Fe, and Cu spectra in PFCNC are almost the same as that of its
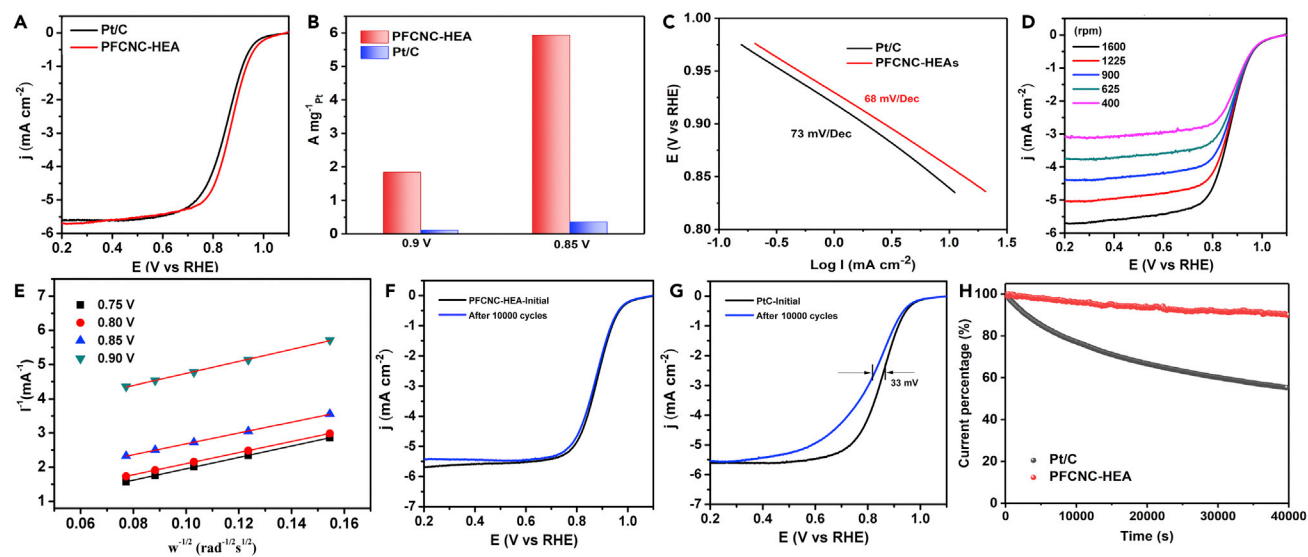
Figure 3. Electrocatalytic performance

(A) ORR polarization curves of the PFCNC-HEA and commercial Pt/C catalysts recorded in O_2-saturated 0.1 M $HClO_4$ solution at room temperature at a scan rate of 10 mV s^{-1} and a rotation rate of 1600 rpm.

(B) Mass activities at 0.9 V vs RHE and (C) Tafel plots. (D) ORR polarization curves of the PFCNC-HEA at different rotation rates and (E) the corresponding Koutecky-Levich plots. ORR polarization curves for (F) the PFCNC-HEA and (G) Pt/C before and after 10,000 cycles.

(H) Normalized chronoamperometric curves of the PFCNC-HEA and Pt/C catalysts at a constant potential at 0.7 V.

corresponding pure metal foil. That is to say, Pt, Co, Ni, Fe, Cu in PFCNC-HEA exhibit a metallic state. The slight deviation of spectra may be caused by the ligand effect, in which the electrons of non-noble metals shift to more electronegative Pt.[38,39] Figures 2D–2F, S6C, and S6D show Fourier transform extended X-ray absorption spectroscopy fine structure (FT-EXAFS) spectra of Pt, Co, Ni, Cu, and Fe, respectively, to further determine the coordination structure of these five metallic elements in PFCNC-HEA and relevant control samples. The experimental k2-weighted EXAFS oscillations of Pt, Co, Ni, Fe, and Cu K-edge are shown in Figure S7 The distance of the first shells (Pt-Pt) in PFCNC-HEA is a little shorter than that of its element metals, attributed to the smaller coordinated transition metal atomic radius. The distance and amplitude are almost identical for the Pt, Co, Ni, Fe, and Cu, indicating Pt, Co, Ni, Fe, and Cu have an identical local atomic structure and coordinated enviroment in PFCNC-HEA. Hence the EXAFS analysis suggests that Pt, Co, Ni, Fe, and Cu in PFCNC-HEA form a solid-solution phase structure without elemental segregation.

X-ray photoelectron spectroscopy (XPS) measurements were used to detect the chemical states. Figures S8A–S8E display the XPS spectra of Ni 2p, Co 2p, Cu 2p, Fe 2p, and Pt 4f, respectively, for the PFCNC-HEA sample. Although there are slight shifts of peaks, the Pt 4f$_{7/2}$ peak at 71.8 eV, Ni 2p$_{3/2}$ peak at 853.7 eV, Co 2p$_{3/2}$ peak at 779.5 eV, Cu 2p$_{3/2}$ peak at 932.3 eV, and Fe2p$_{3/2}$ peak at 710.0 eV, can be attributed the metal Pt^0, Ni^0, Co^0, Cu^0, and Fe^0, respectively, which is consistent with the results of XANES measurements.[4,40,41] In addition, the core energy level of Pt in PFCNC-HEA shifts to lower binding energy compared with that of Pt/C. It can be deduced to be the electron donation from non-noble metals to Pt caused by the ligand effect. The ligand effect can downshift the d-band center of Pt to some suitable extent, thus tuning the affinity between Pt and oxygen intermediates, which is beneficial for the enhancement of ORR activity.[39,42,43]

The electrocatalytic activity of the PFCNC-HEA toward ORR was investigated using a three-electrode system in 0.1 M $HClO_4$ electrolyte at room temperature. As a reference, the 20 wt % commercial Pt/C was also measured under the same measurement conditions. Figure 3A shows the ORR polarization curves of the PFCNC-HEA and Pt/C. The half-wave potential ($E_{1/2}$) of PFCNC-HEA is 0.88 V, which is higher than that of Pt/C (0.85 V). The kinetic currents at 0.9 V vs RHE on the polarization curve were normalized by Pt loading and ECSA to obtain the mass activities (Figure 3B) and specific activities (Figure S10), respectively. It can be found that the mass activity of PFCNC-HEA reaches 1.73 A mg^{-1}$_{Pt}$, which is 15.8 times higher than

that of the state-of-art Pt/C (0.116 A mg^{-1}$_{Pt}$). In addition, its initial potential is about 40 mV higher than that of Pt/C, indicating better intrinsic activity. The specific activity of PFCNC-HEA is up to 2.7 mA cm^{-1}. The Tafel plots of PFCNC-HEA and Pt/C in Figure 3C exhibit a lower Tafel slope (68 mV dec^{-1}) for PFCNC-HEA than that (73 mV dec^{-1}) of Pt/C, indicating that the PFCNC-HEA exhibits more outstanding ORR kinetics. The rotation rate-dependent current-potential curves of PFCNC-HEA are displayed in Figure 3D, and the corresponding Koutecky-Levich plots are shown in Figure 3E. The polarization curves at different rotation speeds under the same potential show a good linear relationship, and the fitting lines are basically parallel. The number of electrons transferred (n) was determined to be approximately 4, demonstrating that the PFCNC-HEA conducts an efficient four-electron mechanism and O_2 is almost completely reduced to H_2O on the surface (Figure S11).

To evaluate the electrochemical stability of the PFCNC-HEA, an accelerated durability test (ADT) was carried out in the range of 0.6 and 1.1 V (vs. RHE) in O_2 saturated 0.1 M $HClO_4$ electrolyte at room temperature. Figures 3F and 3G show the ORR polarization curves after 10k cycles of ADT for PFCNC-HEA and Pt/C, respectively. The PFCNC-HEA catalyst shows a slight decrease in diffusion-limited current, and the $E_{1/2}$ only decays by 3 mV after the ADT test. For commercial Pt/C catalysts, the $E_{1/2}$ attenuation was as high as 33 mV. The mass activity of PFCNC-HEA remains 92% (1.64 A mg^{-1}$_{Pt}$) after 10k cycles of ADT, much higher than that of Pt/C (76% of initial, Figure S12). Compared with the recent noble metal-based catalysts, it has obvious advantages. Furthermore, chronoamperometric measurements were also used to further study the stability of these catalysts at 0.7 V with 1600 rpm (Figure 3H). After 40,000 s of continuous oxygen reduction, it maintains up to 90.23% of the initial current, far surpassing 55.34% of commercial Pt/C. Meanwhile, the ECSA of Pt/C shows a rapid decline after the ADT test (From 68.7 m^2 g^{-1} to 28.3 m^2 g^{-1}), as shown in Figure S14. Nevertheless, the ECSA of the PFCNC-HEA catalyst exhibits no substantial attenuation (Figure S13) The results indicate that the PFCNC-HEA catalyst possesses higher stability in an acidic electrolyte compared to commercial Pt/C catalysts. Figure S15 shows the XPS spectra of PFCNC-HEA nanoparticles after ADT. The peak positions of the five elements are basically consistent with those of the pristine samples of the corresponding elements. The morphology and composition of PFCNC-HEA were investigated to account for the durability of the PFCNC-HEA catalyst (Figure S20). The PFCNC-HEA catalyst shows no obvious aggregation and uniform element distribution with the atomic ratio of HEAs after the ADT test. It could be deduced that the high entropy effect of the HEA catalyst is responsible for the highest catalytic durability of PFCNC-HEA. In addition, the structure and electrochemical properties synthesized at different temperatures were explored (Figures S16 and S17). It was found that the phase of the particles was the purest and the performance was the best at the reduction temperature of 700 °C. Meanwhile, Pt-based binary, ternary and quaternary alloys of corresponding elements were successfully prepared as reference samples, as shown in Figure S18. It can be seen that these non-noble metals can be well alloyed with Pt without obvious phase separation. Nevertheless, their $E_{1/2}$ and peak starting potential are lower than those of PFCNC-HEA samples, which further indicates that the high entropy effect is helpful to improve the ORR catalytic activity of Pt-based catalysts (Figure S19).

Figure 4A shows the metal dissolution energy of the PFCNC-HEA and the corresponding pure metal. As we have known, some alloy catalysts, especially those containing iron, have good electrocatalytic activity toward ORR in half-cell, but their electrochemical performance in the practical cell is not satisfactory due to the dissolution of the secondary components.[44] The dissolution energy of Fe in PFCNC-HEA become positive (1.54 eV), in great contrast to the negative value (−0.465 eV) of that in pure Fe metal, demonstrating that the auto-dissolution of Fe is effectively inhibited through the high entropy effect of PFCNC-HEA. Furthermore, the dissolution energies of all the elements in PFCNC-HEA are positive (>1 eV), which further confirms the excellent stability of PFCNC-HEA. ICP-AES also did not detect transition metal ions in the electrolyte of the electrolytic cell.

The electron amount of surface atoms in the PFCNC-HEA and the corresponding pure metal obtained from Bader charge analysis is depicted in Figure 4B. It can be found that the electron amount of Fe, Co, and Ni in PFCNC-HEA is a little lower than that of corresponding pure metals, while the electron amount of Cu in PFCNC-HEA is a little higher than that of its pure metal, especially for Pt, which is consistent with the results of XPS and XANES measurements. The change of the electron amount of surface atoms results from the ligand effect and electronegativity of different atoms (Pt:2.2, Cu:1.9, Ni:1.88, Co:1.80, Fe:1.83), which will lead to the change in the electronic structure, affect the electrocatalytic activity of the catalyst and the
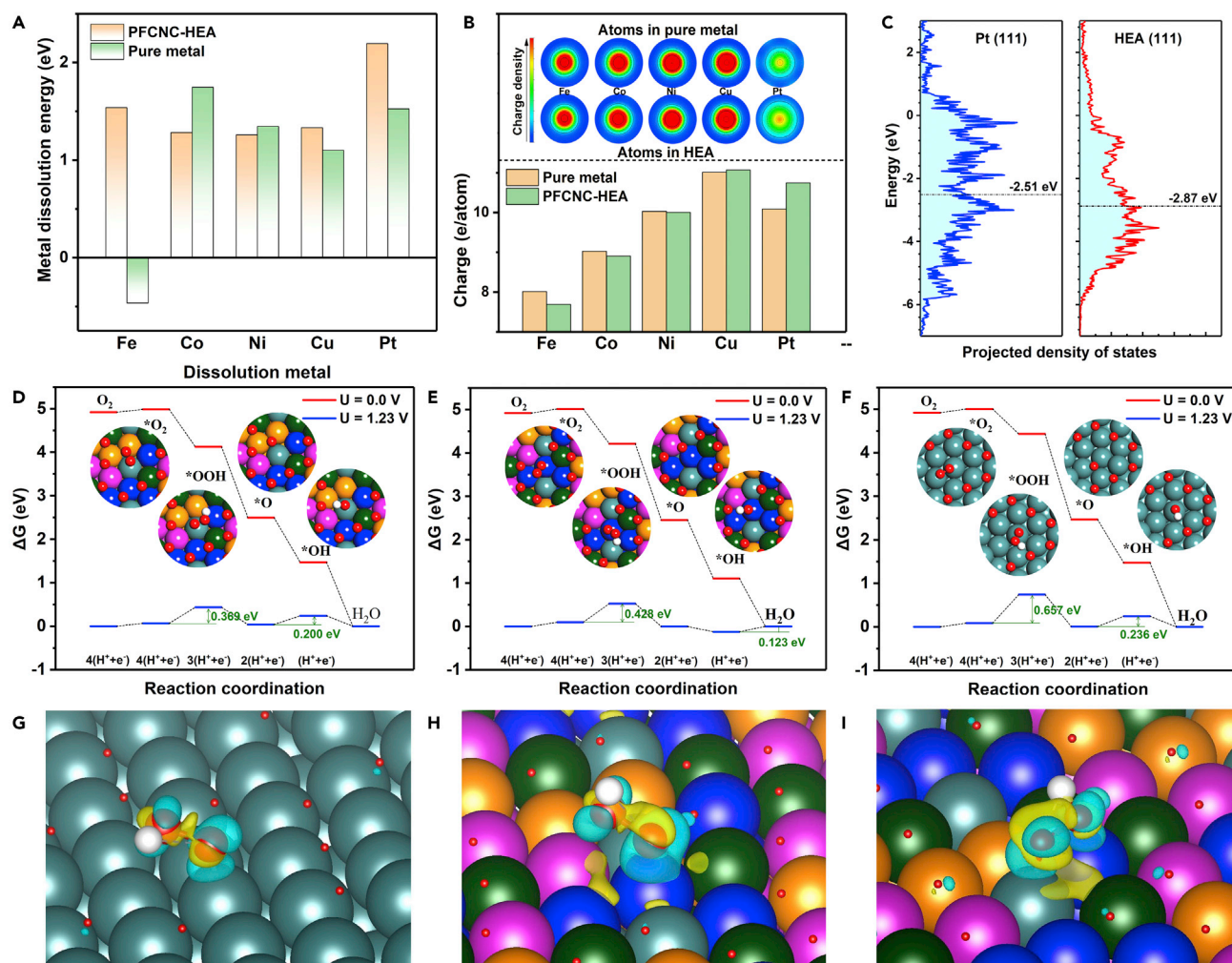
Figure 4. Theoretical calculation of reaction path

(A) The metal dissolution energy of the PFCNC-HEA and the corresponding pure metal.

(B) Electron amount of corresponding surface atoms in the PFCNC-HEA and the corresponding pure metal obtained from Bader charge analysis.

(C) Projected electronic density of states of the d-band for the surface Pt atoms in the pure Pt (111) and PFCNC-HEA (111) surface systems. The free energies of intermediates for the ORR steps of PFCNC-HEA (111) at (D) route 1 and (E) route 2.

(F) The free energies of intermediates for Pt (111). Differential charge density ($\Delta \rho = \rho_{*OOH} - \rho_* - \rho_{OOH}$) of OOH adsorbed system at (G) Pt (111), (H) route 1 and (I) route 2 of PFCNC-HEA (111) with the same isosurface level of 0.0027 e/Bohr^3 isosurface. (green:Pt, blackish green:Fe, pink:Cu, orange:Cu, blue:Co).

stability of catalyst.[45,46] Therefore, projected electronic density of state of the d-band for the surface Pt atoms in the PFCNC-HEA (111) surface system was calculated by density functional theory (DFT). As depicted in Figure 4C, the d-band center of PFCNC-HEA (111) moves to negative energy by 0.36 eV relative to that of pure Pt (111) due to the ligand effect. According to Norskov's work,[47,48] the catalysis activity for the ORR at 0.9 V reaches the maximum when the d-band center position downshifts by about 0.3 eV relative to pure Pt. Therefore, the decrease in the d-band center will alleviate the excessive combination of surface oxygen, move the oxygen chemisorption energy, ΔE_O, to the optimal value and enhance the catalysis activity of PFCNC-HEA.

Further insights into the ORR mechanism, the free energy profiles of PFCNC-HEA and pure Pt were calculated. The reaction intermediates *O2, *OOH, *O, and *OH are involved in the four-electron associative mechanism. There are many surface sites in high entropy alloys, we select typical sites to study their reaction paths in detail. After comparing the adsorption energies of different adsorption configurations, Pt -M and M-M sites bridge absorption (M: transition metals) are set as route 1 (Figure 4D) and route 2 (Figure 4E), respectively. According to previous work, the corresponding O coverage of Pt surface at 1.23 V in
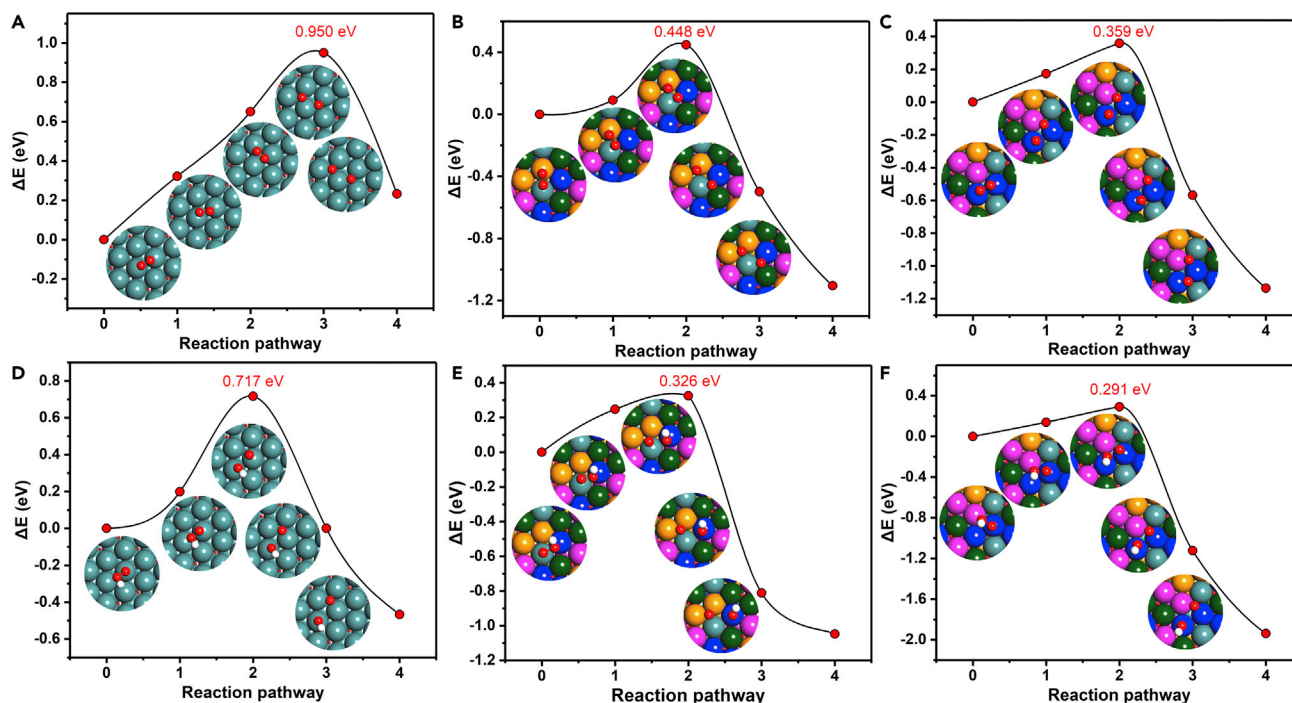
Figure 5. Kinetic study of O-O bond scission

The activation barriers for the O-O bond scission of $*O_2$ at (A) Pt (111) surface, PFCNC-HEA surface (111) for (B) route 1 and (C) route 2. The activation barriers for the O-O bond scission of $*OOH$ at (D) Pt (111) surface, PFCNC-HEA surface for (E) route 1, and (F) for route 2.

the acid environment is about 1/2 monolayer. Thus, about 1/2 monolayer O coverage was considered in our calculations.[49] At equilibrium potential (1.23 V vs. RHE) with 1/2 monolayer O coverage, it shows that the formation of $*OOH$ is the rate-limiting step, regardless of PFCNC-HEA (111) or Pt (111) surface. Both of the formation of $*OOH$ on the PFCNC-HEA (111) surface for route 1 and route 2 are endothermic with $\Delta G = 0.369$ eV and 0.428 V, respectively, which are much lower than that on the Pt (111) surface (0.657 eV, Figure 4F). The result demonstrates a more thermodynamically favorable process and multiple ORR active sites exist on the PFCNC-HEA (111) surface.

Since the formation of $*OOH$ is the rate-limiting step, the interaction between OOH and the surface was investigated to further reveal the mechanism of the thermodynamically favorable process of PFCNC-HEA (111). Figures 4H and 4I show the charge transfer between PFCNC-HEA(111) and OOH in the way of route 1 and route 2, respectively, where the isosurface in yellow and blue represent the charge accumulation and depletion, respectively, compared with the system before adsorption. The charge transfer for OOH at PFCNC-HEA (111) surface is more obvious than that at Pt (111) surface (Figure 4G), indicating stranger interaction between PFCNC-HEA (111) and OOH. Thus, the energy of the $*OOH$ state in the PFCNC-HEA (111) case is lower than that in Pt (111) case, resulting in a smaller ΔG value associated with the formation of $*OOH$. Moreover, as for the Pt (111) surface, charge transfer only can be observed on one Pt atom closest to the adsorbate. In contrast, several transition metal atoms at PFCNC-HEA (111) surface are involved in the charge transfer, indicating a synergistic effect among several transition metal elements (Pt, Fe, Co, Ni, Cu) in the adsorption of OOH at PFCNC-HEA (111) surface.

Additionally, the dynamic processes of O-O bond scission are also investigated. Since the O-O bond nonelectrochemical scission is not potential dependent, the activation barrier reflects the intrinsic reaction efficiency.[50] The activation barriers for O-O bond scission of $*O_2$ and $*OOH$ at Pt (111) surface with 1/16 O coverage are 0.658 (Figure S22A) and 0.592 eV (Figure S22B), respectively. As the O coverage rises to 1/2, the activation barriers for the O-O bond scission of $*O_2$ and $*OOH$ at Pt (111) surface are 0.950 eV (Figure 5A) and 0.717 eV (Figure 5D), respectively. However, the activation barriers for the O-O bond scission of $*O_2$ at PFCNC-HEA (111) surface with 1/2 O coverage range are only 0.448 eV for route 1 (Figure 5B) and 0.359 eV for route 2 (Figure 5C). Additionally, the activation barriers for the O-O bond scission of $*OOH$ at
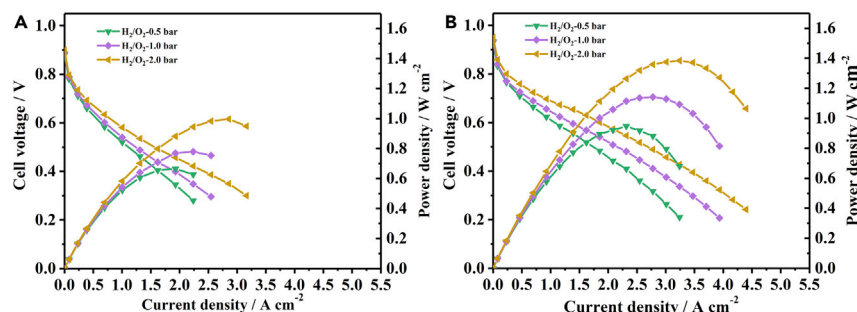
Figure 6. Fuel cell applications
The H_2-O_2 fuel cell i-V polarization and power density of (A) commercial Pt/C and (B) PFCNC-HEA.

PFCNC-HEA (111) also down to 0.326 eV for route 1 (Figure 5E) and 0.291 eV for route 2 (Figure 5F). Easier O-O scission dynamic processes contribute to the efficient ORR activity.[51]

To further corroborate its significant ORR activity, the PFCNC-HEA catalyst incorporated the membrane electrode assembly (MEA) as a cathode and tested its practical H_2-O_2 fuel-cell performance in PFMFC. For comparison, the Pt/C catalyst was also tested at the same condition. The MEA was tested at different partial pressures with a cathodic Pt loading of 0.03 mg_{Pt} cm^{-2}. As shown in Figure 6A, the maximum power densities of the H_2-O_2 fuel cell for Pt/C are 0.66, 0.78, and 0.99 W cm^{-2} with the partial pressure at 0.5, 1.0, and 2.0 bar, respectively. However, the maximum power densities of PFCNC-HEA are up to 0.94, 1.14, and 1.38 W cm^{-2} at 0.5, 1.0, and 2.0 bar, respectively (Figure 6B). Furthermore, the open-cell voltage of the PFCNC-HEA is up to 0.95 V, demonstrating a high intrinsic ORR catalytic activity. PFCNC-HEA shows a current density of 1.85 A/cm^{-2} at 0.6 V, much higher than that of Pt/C (1.0 A/cm^{-2} at 0.6 V). The above results show that PFCNC-HEA shows excellent practical fuel cell performance.

Conclusions

In summary, uniform and small-sized PFCNC-HEA nanoparticles were prepared via an impregnation reduction method. X-ray-based techniques and electron microscopy studies confirmed the high-entropy solid solution PFCNC-HEA nanoparticles have a homogeneous element distribution. The as-obtained PFCNC-HEA exhibits significantly better mass activity and durability than the state-of-art commercial Pt/C catalyst. The excellent durability is attributed to the high entropy effect caused by the increased number of components. Meanwhile, the optimization of the surface electronic structure downshifts the d-band center to enhance the ORR activity. The optimized surface electronic structure decreased the activation barriers for the O-O bond scission to significantly increased the reaction rate of the ORR process and promoted the formation of multiple ORR active sites. Additionally, PFCNC-HEA delivers a maximum power density of 1.38 W cm^{-2} at 2.0 bar in acidic PEMFCs. Therefore, this research demonstrates the great potential of HEAs in the field of electrocatalysis.

Limitations of the study

This synthesis method can only be biased toward the preparation of a low loading catalyst. When the metal load is increased, the particle size will grow significantly.

STAR★METHODS

Detailed methods are provided in the online version of this paper and include the following:

- KEY RESOURCES TABLE
- RESOURCE AVAILABILITY
  - Lead contact
  - Materials availability
  - Data and code availability
- METHOD DETAILS
  - Synthesis of PFCNC-HEA
  - Characterization

○ Electrochemical measurements
○ Computational details
○ Single fuel cell preparation and test

SUPPLEMENTAL INFORMATION

ACKNOWLEDGMENTS

AUTHOR CONTRIBUTIONS

T. C. designed the study. F. H. conducted DFT theoretical calculation. J. Q. and X. L. provided STEM test. Y. W. carried out the fuel cell test. G. F., J. S., and T. Y. helped analyze test results. D. X. and L. C. supervised the project.

DECLARATION OF INTERESTS

The authors declare no competing interests.

INCLUSION AND DIVERSITY

We support the inclusive, diverse, and equitable conduct of research.

REFERENCES

1. Debe, M.K. (2012). Electrocatalyst approaches and challenges for automotive fuel cells. Nature 486, 43–51. https://doi.org/10.1038/nature11115.

2. Zhang, D., Wu, F., Peng, M., Wang, X., Xia, D., and Guo, G. (2015). One-step, facile and ultrafast synthesis of phase- and size-controlled Pt-Bi intermetallic nanocatalysts through continuous-flow microfluidics. J. Am. Chem. Soc. 137, 6263–6269. https://doi.org/10.1021/jacs.5b01088.

3. Xia, Z., An, L., Chen, P., and Xia, D. (2016). Non-Pt nanostructured catalysts for oxygen reduction reaction: synthesis, catalytic activity and its key factors. Adv. Energy Mater. 6, 1600458. https://doi.org/10.1002/aenm.201600458.

4. Li, M., Wang, Y., Zheng, Y., Fu, G., Sun, D., Li, Y., Tang, Y., and Ma, T. (2020). Gadolinium-induced valence structure engineering for enhanced oxygen electrocatalysis. Adv. Energy Mater. 10, 1903833. https://doi.org/10.1002/aenm.201903833.

5. Bu, L., Zhang, N., Guo, S., Zhang, X., Li, J., Yao, J., Wu, T., Lu, G., Ma, J.-Y., and Su, D. (2016). Biaxially strained PtPb/Pt core/shell nanoplate boosts oxygen reduction catalysis. Science 354, 1410–1414.

6. Chen, C., Kang, Y., Huo, Z., Zhu, Z., Huang, W., Xin, H.L., Snyder, J.D., Li, D., Herron, J.A., Mavrikakis, M., et al. (2014). Highly crystalline multimetallic nanoframes with three-dimensional electrocatalytic surfaces. Science 343, 1339–1343.

7. Xiao, M., Zhu, J., Feng, L., Liu, C., and Xing, W. (2015). Meso/macroporous nitrogen-doped carbon architectures with iron carbide encapsulated in graphitic layers as an efficient and robust catalyst for the oxygen reduction reaction in both acidic and alkaline solutions. Adv. Mater. 27, 2521–2527. https://doi.org/10.1002/adma.201500262.

8. Li, J., Chen, M., Cullen, D.A., Hwang, S., Wang, M., Li, B., Liu, K., Karakalos, S., Lucero, M., Zhang, H., et al. (2018). Atomically dispersed manganese catalysts for oxygen reduction in proton-exchange membrane fuel cells. Nat. Catal. 1, 935–945. https://doi.org/10.1038/s41929-018-0164-8.

9. Lv, G., Wu, Y., Wang, Y., Kang, W., Zhang, H., Zhou, M., Huang, Z., Li, J., Guo, Z., and Wang, Y. (2020). Rational design of perfect interface coupling to boost electrocatalytical oxygen reduction. Nano Energy 76, 105055. https://doi.org/10.1016/j.nanoen.2020.105055.

10. Kulkarni, A., Siahrostami, S., Patel, A., and Nørskov, J.K. (2018). Understanding catalytic activity trends in the oxygen reduction reaction. Chem. Rev. 118, 2302–2312.

11. Seh, Z.W., Kibsgaard, J., Dickens, C.F., Chorkendorff, I., Nørskov, J.K., and Jaramillo, T.F. (2017). Combining theory and experiment in electrocatalysis: insights into materials design. Science 355, eaad4998. https://doi.org/10.1126/science.aad4998.

12. Ma, Z., Li, S., Wu, L., Song, L., Jiang, G., Liang, Z., Su, D., Zhu, Y., Adzic, R.R., Wang, J.X., and Chen, Z. (2020). NbOx nano-nail with a Pt head embedded in carbon as a highly active and durable oxygen reduction catalyst. Nano Energy 69, 104455. https://doi.org/10.1016/j.nanoen.2020.104455.

13. Yang, X., Wang, Y., Zhang, G., Du, L., Yang, L., Markiewicz, M., Choi, J.-y., Chenitz, R., and Sun, S. (2020). SiO2-Fe/N/C catalyst with enhanced mass transport in PEM fuel cells. Appl. Catal. B Environ. 264, 118523. https://doi.org/10.1016/j.apcatb.2019.118523.

14. Li, C., Iqbal, M., Jiang, B., Wang, Z., Kim, J., Nanjundan, A.K., Whitten, A.E., Wood, K., and Yamauchi, Y. (2019). Pore-tuning to boost the electrocatalytic activity of polymeric micelle-templated mesoporous Pd nanoparticles. Chem. Sci. 10, 4054–4061. https://doi.org/10.1039/c8sc03911a.

15. Wang, F., Fang, B., Yu, X., and Feng, L. (2019). Coupling ultrafine Pt nanocrystals over the Fe2P surface as a robust catalyst for alcohol

fuel electro-oxidation. ACS Appl. Mater. Interfaces 11, 9496–9503. https://doi.org/10.1021/acsami.8b18029.

16. Bing, Y., Liu, H., Zhang, L., Ghosh, D., and Zhang, J. (2010). Nanostructured Pt-alloy electrocatalysts for PEM fuel cell oxygen reduction reaction. Chem. Soc. Rev. 39, 2184–2202. https://doi.org/10.1039/b912552c.

17. Zhang, L., Wang, Q., Li, L., Banis, M.N., Li, J., Adair, K., Sun, Y., Li, R., Zhao, Z.-J., Gu, M., and Sun, X. (2022). Single atom surface engineering: a new strategy to boost electrochemical activities of Pt catalysts. Nano Energy 93, 106813. https://doi.org/10.1016/j.nanoen.2021.106813.

18. Koo, W.T., Millstone, J.E., Weiss, P.S., and Kim, I.D. (2020). The design and science of polyelemental nanoparticles. ACS Nano 14, 6407–6413. https://doi.org/10.1021/acsnano.0c03993.

19. Löffler, T., Meyer, H., Savan, A., Wilde, P., Garzón Manjón, A., Chen, Y.-T., Ventosa, E., Scheu, C., Ludwig, A., and Schuhmann, W. (2018). Discovery of a multinary noble metal-free oxygen reduction catalyst. Adv. Energy Mater. 8, 1802269. https://doi.org/10.1002/aenm.201802269.

20. George, E.P., Raabe, D., and Ritchie, R.O. (2019). High-entropy alloys. Nat. Rev. Mater. 4, 515–534. https://doi.org/10.1038/s41578-019-0121-4.

21. Cantor, B., Chang, I.T.H., Knight, P., and Vincent, A.J.B. (2004). Microstructural development in equiatomic multicomponent alloys. Mater. Sci. Eng. A 375–377, 213–218. https://doi.org/10.1016/j.msea.2003.10.257.

22. Huang, K., Zhang, B., Wu, J., Zhang, T., Peng, D., Cao, X., Zhang, Z., Li, Z., and Huang, Y. (2020). Exploring the impact of atomic lattice deformation on oxygen evolution reactions based on a sub-5 nm pure face-centred cubic high-entropy alloy electrocatalyst. J. Mater. Chem. A 8, 11938–11947. https://doi.org/10.1039/d0ta02125c.

23. Li, H., Han, Y., Zhao, H., Qi, W., Zhang, D., Yu, Y., Cai, W., Li, S., Lai, J., Huang, B., and Wang, L. (2020). Fast site-to-site electron transfer of high-entropy alloy nanocatalyst driving redox electrocatalysis. Nat. Commun. 11, 5437. https://doi.org/10.1038/s41467-020-19277-9.

24. Yao, Y., Liu, Z., Xie, P., Huang, Z., Li, T., Morris, D., Finfrock, Z., Zhou, J., Jiao, M., Gao, J., et al. (2020). Computationally aided, entropy-driven synthesis of highly efficient and durable multi-elemental alloy catalysts. Sci. Adv. 6, eaaz0510.

25. Li, H., Lai, J., Li, Z., and Wang, L. (2021). Multi-Site electrocatalysts boost pH-universal nitrogen reduction by high-entropy alloys. Adv. Funct. Mater. 31, 2106715. https://doi.org/10.1002/adfm.202106715.

26. Xia, Z., and Guo, S. (2019). Strain engineering of metal-based nanomaterials for energy electrocatalysis. Chem. Soc. Rev.

48, 3265–3278. https://doi.org/10.1039/c8cs00846a.

27. Luo, M., and Guo, S. (2017). Strain-controlled electrocatalysis on multimetallic nanomaterials. Nat. Rev. Mater. 2, 17059. https://doi.org/10.1038/natrevmats.2017.59.

28. Wang, D., Chen, Z., Huang, Y.-C., Li, W., Wang, J., Lu, Z., Gu, K., Wang, T., Wu, Y., Chen, C., et al. (2021). Tailoring lattice strain in ultra-fine high-entropy alloys for active and stable methanol oxidation. Sci. China Mater. 64, 2454–2466. https://doi.org/10.1007/s40843-020-1635-9.

29. Zhang, Y., Wang, D., and Wang, S. (2022). High-entropy alloys for electrocatalysis: design, characterization, and applications. Small 18, 2104339. https://doi.org/10.1002/smll.202104339.

30. Wang, D., Chen, Z., Wu, Y., Huang, Y., Tao, L., Chen, J., Dong, C., Singh, C.V., and Wang, S. (2022). Structurally ordered high-entropy intermetallic nanoparticles with enhanced C–C bond cleavage for ethanol oxidation. SmartMat 4, 1–11. https://doi.org/10.1002/smm2.1117.

31. Nandan, R., Raj, G., and Nanda, K.K. (2022). FeCoNiMnCr high-entropy alloy nanoparticle-grafted NCNTs with promising performance in the ohmic polarization region of fuel cells. ACS Appl. Mater. Interfaces 14, 16108–16116. https://doi.org/10.1021/acsami.1c21336.

32. Lai, W., Zhang, B., Hu, Z., Qu, X., Jiang, Y., Wang, Y., Wang, J., Liu, H.K., and Chou, S. (2019). The quasi-Pt-allotrope catalyst: hollow PtCo@single-Atom Pt1 on nitrogen-doped carbon toward superior oxygen reduction. Adv. Funct. Mater. 29, 1807340. https://doi.org/10.1002/adfm.201807340.

33. Zhao, X., Cheng, H., Song, L., Han, L., Zhang, R., Kwon, G., Ma, L., Ehrlich, S.N., Frenkel, A.I., Yang, J., et al. (2020). Rhombohedral ordered intermetallic nanocatalyst boosts the oxygen reduction reaction. ACS Catal. 11, 184–192. https://doi.org/10.1021/acscatal.0c04021.

34. Wang, D., Liu, S., Wang, J., Lin, R., Kawasaki, M., Rus, E., Silberstein, K.E., Lowe, M.A., Lin, F., Nordlund, D., et al. (2016). Spontaneous incorporation of gold in palladium-based ternary nanoparticles makes durable electrocatalysts for oxygen reduction reaction. Nat. Commun. 7, 11941. https://doi.org/10.1038/ncomms11941.

35. Ma, Y., Gao, W., Shan, H., Chen, W., Shang, W., Tao, P., Song, C., Addiego, C., Deng, T., Pan, X., and Wu, J. (2017). Platinum-based nanowires as active catalysts toward oxygen reduction reaction: in situ observation of surface-diffusion-assisted, solid-state oriented attachment. Adv. Mater. 29, 1703460. https://doi.org/10.1002/adma.201703460.

36. Xie, P., Yao, Y., Huang, Z., Liu, Z., Zhang, J., Li, T., Wang, G., Shahbazian-Yassar, R., Hu, L., and Wang, C. (2019). Highly efficient decomposition of ammonia using high-entropy alloy catalysts. Nat. Commun. 10,

4011. https://doi.org/10.1038/s41467-019-11848-9.

37. Zhang, W., Liaw, P.K., and Zhang, Y. (2018). Science and technology in high-entropy alloys. Sci. China Mater. 61, 2–22. https://doi.org/10.1007/s40843-017-9195-8.

38. Duchesne, P.N., Chen, G., Zheng, N., and Zhang, P. (2013). Local structure, electronic behavior, and electrocatalytic reactivity of CO-reduced platinum–iron oxide nanoparticles. J. Phys. Chem. C 117, 26324–26333. https://doi.org/10.1021/jp4093496.

39. Tian, X., Zhao, X., Su, Y.-Q., Wang, L., Wang, H., Dang, D., Chi, B., Liu, H., Hensen, E.J.M., and Lou, X.W.D. (2019). Engineering bunched Pt-Ni alloy nanocages for efficient oxygen reduction in practical fuel cells. Science 366, 850–856.

40. Zhan, C., Xu, Y., Bu, L., Zhu, H., Feng, Y., Yang, T., Zhang, Y., Yang, Z., Huang, B., Shao, Q., and Huang, X. (2021). Subnanometer high-entropy alloy nanowires enable remarkable hydrogen oxidation catalysis. Nat. Commun. 12, 6261. https://doi.org/10.1038/s41467-021-26425-2.

41. Tu, W., Luo, W., Chen, C., Chen, K., Zhu, E., Zhao, Z., Wang, Z., Hu, T., Zai, H., Ke, X., et al. (2019). Tungsten as "adhesive" in Pt2CuW 0.25 ternary alloy for highly durable oxygen reduction electrocatalysis. Adv. Funct. Mater. 30, 1908230. https://doi.org/10.1002/adfm.201908230.

42. Greeley, J., Stephens, I.E.L., Bondarenko, A.S., Johansson, T.P., Hansen, H.A., Jaramillo, T.F., Rossmeisl, J., Chorkendorff, I., and Nørskov, J.K. (2009). Alloys of platinum and early transition metals as oxygen reduction electrocatalysts. Nat. Chem. 1, 552–556. https://doi.org/10.1038/nchem.367.

43. Kong, F., Ren, Z., Norouzi Banis, M., Du, L., Zhou, X., Chen, G., Zhang, L., Li, J., Wang, S., Li, M., et al. (2020). Active and stable Pt–Ni alloy octahedra catalyst for oxygen reduction via near-surface atomical engineering. ACS Catal. 10, 4205–4214. https://doi.org/10.1021/acscatal.9b05133.

44. Qu, X., Han, Y., Chen, Y., Lin, J., Li, G., Yang, J., Jiang, Y., and Sun, S. (2021). Stepwise pyrolysis treatment as an efficient strategy to enhance the stability performance of Fe-NX/C electrocatalyst towards oxygen reduction reaction and proton exchange membrane fuel cell. Appl. Catal. B Environ. 295, 120311. https://doi.org/10.1016/j.apcatb.2021.120311.

45. Feng, G., Ning, F., Song, J., Shang, H., Zhang, K., Ding, Z., Gao, P., Chu, W., and Xia, D. (2021). Sub-2 nm ultrasmall high-entropy alloy nanoparticles for extremely superior electrocatalytic hydrogen evolution. J. Am. Chem. Soc. 143, 17117–17127. https://doi.org/10.1021/jacs.1c07643.

46. Feng, G., An, L., Li, B., Zuo, Y., Song, J., Ning, F., Jiang, N., Cheng, X., Zhang, Y., and Xia, D. (2019). Atomically ordered non-precious Co3Ta intermetallic nanoparticles as high-performance catalysts

for hydrazine electrooxidation. Nat. Commun. *10*, 4514. https://doi.org/10.1038/s41467-019-12509-7.

47. Stamenkovic, V., Mun, B.S., Mayrhofer, K.J., Ross, P.N., Markovic, N.M., Rossmeisl, J., Greeley, J., and Nørskov, J.K. (2006). Changing the activity of electrocatalysts for oxygen reduction by tuning the surface electronic structure. Angew. Chem. *118*, 2963–2967. https://doi.org/10.1002/ange.200504386.

48. Nie, Y., Li, L., and Wei, Z. (2015). Recent advancements in Pt and Pt-free catalysts for oxygen reduction reaction. Chem. Soc. Rev. *44*, 2168–2201. https://doi.org/10.1039/c4cs00484a.

49. Russell, A.E., Rossmeisl, J., and Nørskov, J.K. (2008). Electrocatalysis: theory and experiment at the interface. Phys. Chem. Chem. Phys. *10*, 3607–3608. https://doi.org/10.1039/b808799g.

50. Marković, N.M., Schmidt, T.J., Stamenković, V., and Ross, P.N. (2001). Oxygen reduction reaction on Pt and Pt bimetallic surfaces: a selective review. Fuel Cell. *1*, 105–116.

51. Keith, J.A., and Jacob, T. (2010). Theoretical studies of potential-dependent and competing mechanisms of the electrocatalytic oxygen reduction reaction on Pt(111). Angew. Chem. Int. Ed. Engl. *49*, 9521–9525.

STAR★METHODS

KEY RESOURCES TABLE

REAGENT or RESOURCE	SOURCE	IDENTIFIER
Chemicals, peptides, and recombinant proteins		
$H_2PtCl_6 \cdot 6H_2O$	Aladdin Co., Ltd	18497-13-7
Cobalt(II) acetylacetonate	Aladdin Co., Ltd	14024-48-7
Iron(III) acetylacetonate	Aladdin Co., Ltd	14024-18-1
Nickel acetylacetonate	Aladdin Co., Ltd	3264-82-2
Copper acetylacetonate	Aladdin Co., Ltd	13395-16-9
Commercial 20%Pt/C	Johnson Matthey Fuel Cells	Cat#S128513
Perchloric acid (71 wt.%)	Tianjin Zhengcheng	7601-90-3
Nafion Solution (5%)	Macklin	31175-20-9
XC-72	Macklin	1333-86-4

RESOURCE AVAILABILITY

Lead contact
Further information and requests for resources should be directed to and will be fulfilled by the lead contact, Dingguo Xia (dgxia@pku.edu.cn).

Materials availability
This study did not generate new unique reagents. All chemicals were obtained from commercial resources and used as received.

Data and code availability
The published article includes all datasets generated or analyzed during this study.

All data reported in this paper will be shared by the lead contact upon request.

This paper does not report original code.

METHOD DETAILS

Synthesis of PFCNC-HEA
An impregnation reduction strategy is conduced to synthesize PFCNC-HEA nanoparticles supported on Vulcan XC-72 carbon support. In detail, 4.23 mg Co(acac)$_2$, 5.9 mg (Fe(acac)$_3$), 4.36 mg (Ni(acac)$_2$), 4.3 mg (Cu(acac)$_2$) and 0.77 mL of 10 mM $H_2PtCl_6 \cdot 6H_2O$ were first dissolved in 20 mL mixture of water and alcohol. Then, 50 mg Vulcan XC-72 carbon support was dispersed in the solution and ultrasoniced for half an hour. The suspension was heated at 70 °C with magnetic stirring to evaporate solvent. The obtained thick slurry was then transferred into an oven to dry overnight to guarantee a completely drying. After grounding in an agate mortar, the powder was annealed and alloyed at 700 °C for half hour under flowing H$_2$/Ar. After treatment with 0.1M HClO$_4$ solution for half an hour, centrifuge and dry overnight. The as-prepared reference samples with different atomic ratios were synthesized in the same procedure. The reference samples of different synthetic temperatures are also synthesized in the same procedure but except for changing the final calcination temperature. The mixed configuration entropy of HEAs is able to be depicted by the following equation:

$$S = -\sum x_i ln(x_i) \quad \text{(Equation 1)}$$

where R is the molar gas constant, and xi represents the mole fraction of the elemental component.

Characterization

XRD patterns were recorded on an Bruker D8 Focus XRD at a scan rate of $1° \text{ min}^{-1}$ with Cu K radiation. TEM test was carried out using a JEOL 2010F microscope operated at 200 kV. The high-resolution STEM images, STEM-EDX mapping, and line-scan were carried out under a Cs-corrected STEM (FEI Titan Themis Z) operated at 300 kV with a convergence semi-angle of 25 mrad, which was corrected by probe SCOR spherical aberration corrector. ICP-MS was measured on a PerkinElmer NexION 300D ICP-MS. XPS was performed using a VG ESCALAB MKII instrument, which uses Mg Kα X-ray source. The Fe, Co, Ni and Cu K-edge spectra and Pt L_3-edge were collected at in the fluorescence mode at beamline 1W2B with a Si (111) double-crystal monochromator at the Beijing Synchrotron Radiation Facility (BSRF). ATHENA software package was used to analyse the XANES and extended X-ray absorption fine-structure data.

Electrochemical measurements

Electrochemical experiments were tested in a three-electrode cell using a CHI 760E. Glassy carbon rotating disk electrode was served as the working electrode. A Hg/HgSO₄ electrode was used as the reference electrode, and Pt wire were used as the counter electrode. 2mg carbon-supported catalyst was dispersed in the mixture of 490 μL isopropanol, 490 μL deionized water and 20 μL Nafion (5%). The mixture was sonicated for 30 min to obtain a homogeneous catalyst ink. Finally, 2 μL catalyst ink cast onto glassy carbon rotating disk electrode with 4mm diameter and dry naturally. CV curves were conducted in N_2-saturated 0.1 M HClO_4 with a sweep rate 50 mV s^{-1}. The ORR polarization curves were tested in O_2-saturated 0.1 M HClO_4 at a scanning rate of 10 mV s^{-1} with iR drop correction. The accelerated durability test (ADT) was performed at by potential sweeps between 0.6 and 1.1 V for 10000 cycles with 100 mV s^{-1}. And the HER test was conducted at $0.5 \text{ M H}_2\text{SO}_4$ with a scan rate of 2 mV s^{-1}.

Computational details

All the first-principles calculations in this work were performed in the Vienna ab initio simulation package (VASP) 5.4.4. The generalized gradient approximation (GGA) with the Perdew-Burke-Ernzerhof (PBE) exchange correlation functional and a 520 eV cutoff energy for the plane-wave basis set were employed. For all theoretical models, the convergence threshold was set as 10-5 eV in energy and 0.01 eV/Å in force. For the slab models of Pt (111), 4 × 4 repeated unit cell with four atom layers, was used (Figure S21B). The slab model of PFCNC-HEA (111) is obtained by replacing Pt atoms in Pt (111) slab model (Figure S21A). The atomic ratio within the HEA (111) slab model is Fe: Co: Ni: Cu: Pt = 2.0: 2.0: 2.0: 2.0: 1.14, which is basically in accordance with the ICP results. The free energy change of reaction was defined by $\Delta G = \Delta E + \Delta ZPE – T\Delta S$. Herein, ΔE is the change of electronic energy obtained from DFT calculations, ΔZPE is the change of zero-point energy, and ΔS is the entropy difference. And the free energy change with an applied potential was defined by $\Delta G(U) = \Delta G + eU$.

Single fuel cell preparation and test

Catalyst ink for 30% nafion electrodes was made by ultrasonically mixing the catalyst, deionized water, isopropanol, and 5wt% Nafion ionomer solution for 1h. Then the catalyst slurry was applied to the carbon paper by spraying to form the cathode catalyst layer with loading of $0.03 \text{ mg}_{Pt} \text{ cm}^{-2}$. As for anode, t/C (20 wt. % of Pt, JM Hispec3000) was used with loading of $0.1 \text{ mg}_{Pt} \text{ cm}^{-2}$. The prepared cathode and anode were pressed onto the two sides of a Nafion 211 membrane (DuPont) at 120 °C to obtain the membrane electrode assembly. The geometric area of the MEA was 12.25 cm2. The fuel cell performance was measured with 850e Fuel Cell Test Station. The gases were humidified at 80 °C with the flow rate of 0.6 L min-1 for H_2 and 2.6 L min-1 for O_2. The absolute pressure was 1.0 bar for H_2 and 0.5–2 bar for O_2.